Photophysics of GaN single-photon emitters in the visible spectral range

Amanuel M. Berhane,[1] Kwang-Yong Jeong,[2,3] Carlo Bradac,[1] Michael Walsh,[2]
Dirk Englund,[2] Milos Toth,[1] and Igor Aharonovich[1,*]

[1]*School of Mathematical and Physical Sciences, University of Technology Sydney, Ultimo, New South Wales, 2007, Australia*
[2]*Department of Electrical Engineering and Computer Science, MIT, Cambridge, Massachusetts 02139, USA*
[3]*Department of Nano Science and Technology, Gachon University, Gyeonggi-do 13120, Republic of Korea*

(Received 29 August 2017; revised manuscript received 29 March 2018; published 12 April 2018)

In this work, we present a detailed photophysical analysis of recently discovered, optically stable single-photon emitters (SPEs) in gallium nitride (GaN). Temperature-resolved photoluminescence measurements reveal that the emission lines at 4 K are three orders of magnitude broader than the transform-limited width expected from excited-state lifetime measurements. The broadening is ascribed to ultrafast spectral diffusion. The photophysical study on several emitters at room temperature (RT) reveals an average brightness of (427 ± 215) kCounts/s. Finally, polarization measurements from 14 emitters are used to determine visibility as well as dipole orientation of defect systems within the GaN crystal. Our results underpin some of the fundamental properties of SPEs in GaN both at cryogenic and RT, and define the benchmark for future work in GaN-based single-photon technologies.

DOI: 10.1103/PhysRevB.97.165202

I. INTRODUCTION

Single-photon emitters (SPEs) are fundamental building blocks for application in quantum communication [1], quantum cryptography [2], quantum states distribution [3,4], and information processing [5–7]. Single photons can be produced using nonlinear processes such as spontaneous parametric down conversion [8,9]; on-demand single photons can also be generated using quantum dots [10,11], single molecules [12,13], or defects in solids [5,14]. The latter are promising candidates for scalable quantum nanophotonics and for studying light-matter interaction as they can be easily integrated into photonic crystals and waveguides [14–18]. In particular, SPEs operating at room temperature are extremely desirable for practical devices. Among the most studied room-temperature SPEs, color centers in diamond [7,18–21], silicon carbide [22–25], zinc oxide [26–28], and—-more recently—-hexagonal boron nitride [29] are shaping the field. Concurrently, there is a growing push toward identifying and characterizing new emitters with analogous or even superior properties and in material systems with well-established growth and nanofabrication protocols.

Gallium nitride (GaN) is one such material. For instance, GaN quantum dots (QDs) have been incorporated into nanoscale pillars to generate bright single-photons sources in the UV spectral range at cryogenic temperatures and, to some extent, at room temperature (RT) [30–32]. It has also recently been shown that defects in GaN can act as polarized, bright SPEs that operate at RT emitting in the visible [33,34] and telecom spectral range [35]. While the origin of the SPEs is still under debate, it is believed these are point defects located near cubic inclusions in a hexagonal lattice. These SPEs are observed in commercial wafers, which are important for integration with optoelectronic devices and circuits. However, more work is needed to improve our current understanding of the photophysics, atomic structure, and technological potential of SPEs in GaN. In particular, understanding their level structure and the performance at cryogenic temperatures is important before these emitters can be used to perform advanced quantum optics experiments such as photon interference and entanglement.

In this work, we perform a detailed photophysical analysis of optically stable SPEs in GaN. We present cryogenic-temperature spectroscopic data, and a room-temperature analysis of the saturation behavior and transition kinetics for a range of emitters; we also provide detailed polarization measurements at RT.

II. EXPERIMENTAL SETUP

The sample used in this study is a commercially available 4-μm (2-μm p-type/2-μm undoped) GaN crystal grown on sapphire, obtained from Suzhou Nanowin Science and Technology Co., Ltd. The cryogenic-temperature measurements are carried out by placing the sample on an XYZ piezo stage, located in a closed-cycle Montana cryostat system with temperature control down to 4 K. All spectroscopy and second-order correlation measurements are carried out using a confocal microscope with an integrated Hanbury-Brown and Twiss interferometer. A cw laser (wavelength 532 nm) is used for excitation. The beam is focused to a spot size of $\sim$400 nm through a 100$\times$ objective with a numerical aperture (NA) of 0.9. RT polarization spectroscopy is carried out using the confocal microscope where the polarization of the excitation laser is controlled by placing a half-wave plate into the optical path, while a visible polarizer is used in collection to monitor the emission polarization. Quarter-wave plates are used both on the excitation and detection paths to correct for birefringent components. Lifetime measurements are carried out using a pulsed laser (pulse width 32 ps) with a wavelength of 532 nm.

*Corresponding author: igor.aharonovich@uts.edu.au

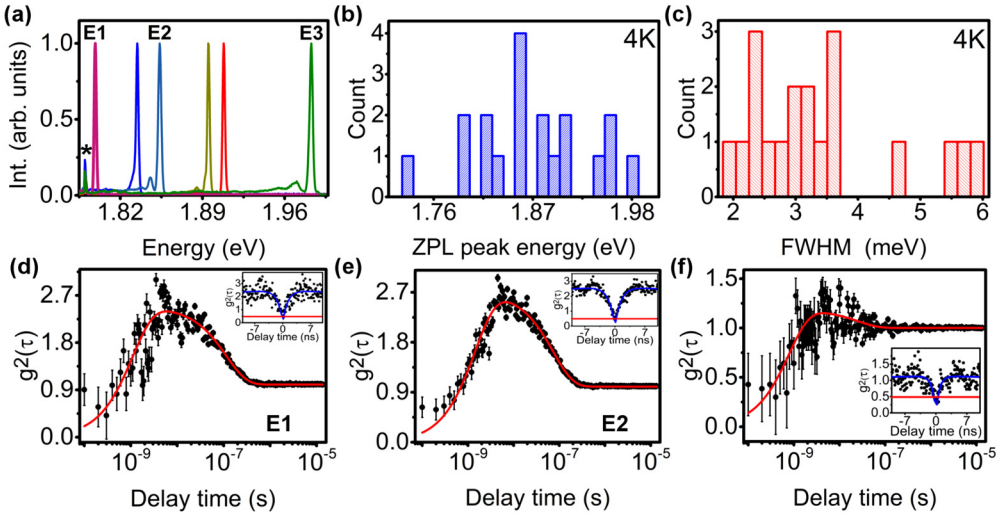

FIG. 1. Low-temperature (4 K) spectroscopy and photon emission statistics of quantum emitters in GaN. (a) Representative spectra from six emitters with ZPL peak energies of 1.796 eV (E1), 1.834 and 1.852 eV (E2), and 1.895, 1.908, and 1.981 eV (E3). (b) ZPL peak energy distribution of 19 emitters with mean value of (1.869 ± 0.064) eV. (c) Histogram showing the FWHM distribution of the emitters in (b) with mean linewidth value of (3.39 ± 1.12) meV. All measurements were taken with an excitation laser power of 100 μW. (d)–(f) Second-order autocorrelation measurements for the three emitters labeled E1–E3 in (a) under an excitation power of 50 μW over long delay times. Inset are the $g^2(\tau)$ functions of the same emitters near zero delay time. The curves are fitted with three-level, second-order autocorrelation functions and show that the emitters E1–E3 are single photon emitters with $g^2(\tau = 0)$ values: 0.36, 0.48, and 0.31, respectively.

III. RESULTS AND DISCUSSION

We start by surveying single emitters at cryogenic temperatures. Figure 1(a) shows spectra for six emitters selected at random using an excitation laser power of 100 μW, at 4 K. A distinct zero-phonon line (ZPL) is obtained for each one of the emitters. The distribution of ZPL peak energy is shown in Fig. 1(b) and was obtained by analyzing a total of 19 emitters. The ZPL position ranges from 1.736 to 1.983 eV with a mean of (1.869 ± 0.064) eV. The histogram is similar to that reported for RT GaN (which has a mean of ~1.824 eV) [33], illustrating that the mechanism responsible for the observed ZPL energy range is unaffected by temperature. This is consistent with—-and expected from—-the interpretation that the energy range corresponds to variations in the positions of individual emitters in cubic inclusions in wurtzite GaN [33]. A histogram of the full width at half maximum (FWHM) of the 19 emitters at 4 K is shown in Fig. 1(c) with the mean linewidth of (3.39 ± 1.12) meV, which is approximately 7 times smaller than the previously measured mean linewidth at RT [33]. The additional narrow peak seen at 1.789 eV in Fig. 1(a) (indexed with asterisk) is the Cr impurity emission from the sapphire substrate.

To further characterize the SPEs, we focus on emitters E1, E2, and E3 which approximately span the observed ZPL range, as indicated in Fig. 1(a), and have ZPL FWHMs of 1.796 eV (1.6 meV), 1.852 eV (2.4 meV), and 1.981 eV (2.3 meV), respectively. To better visualize the ZPL coupling to phonon sidebands (PSB) of E1, E2, and E3, the respective spectra are replotted on the logarithmic y axis as shown in Fig. S1 (see Supplemental Material [36]). This indicates that most of the emission from GaN emitters comes from the ZPL with very weak coupling to the PSB. The emitters are photostable, as illustrated by the fluorescence time-trace measurements shown in Fig. S2 [36]. Figures 1(d)–1(f) show second-order autocorrelation measurements for correlation times of up to 15 μs, with the inset showing corresponding short-delay time $g^{(2)}(\tau)$ characteristics. Fitting the second-order autocorrelation measurements for the three emitters with Eq. (1) yields $g^{(2)}(\tau = 0)$ values for of 0.36, 0.48, and 0.31, respectively. The deviations from zero are due to background fluorescence and detector jitter (~600 ps). The data can be fitted optimally with minimum chi-squared by a three-level model with a long-lived metastable state [34]:

$$g^2(\tau) = 1 - (1 + a)e^{-|\tau|/|\tau_1|} + ae^{-|\tau|/|\tau_2|}, \qquad (1)$$

where a, τ_1, and τ_2 are the branching ratio of rate coefficients, antibunching, and bunching fit parameters, respectively. The values of a, τ_1, and τ_2 obtained by after the fitting of $g^2(\tau)$ are summarized in Table I. Although the bunching behavior [seen as a peak in each $g^2(\tau)$ profile] is different for each one of the emitters, it is clear that a shelving state observed at RT [33] persists at cryogenic temperatures. Extended photon correlation measurements of up to 0.1 s (see Fig. S3 of Supplemental Material [36]) confirm the absence of additional, longer-lived metastable states, with the $g^2(\tau)$ profiles remaining constant for up to 0.1 s.

TABLE I. Parametric values for a, τ_1, and τ_2 obtained by fitting the second-order autocorrelation functions of E1, E2, and E3, assuming three-level system dynamics.

	E1	E2	E3
a	1.48 ± 0.03	1.71 ± 0.03	0.18 ± 0.04
τ_1 (ns)	1.13 ± 0.13	1.49 ± 0.11	0.79 ± 0.16
τ_2 (ns)	114.92 ± 3.2	74.26 ± 3.09	26.23 ± 7.49

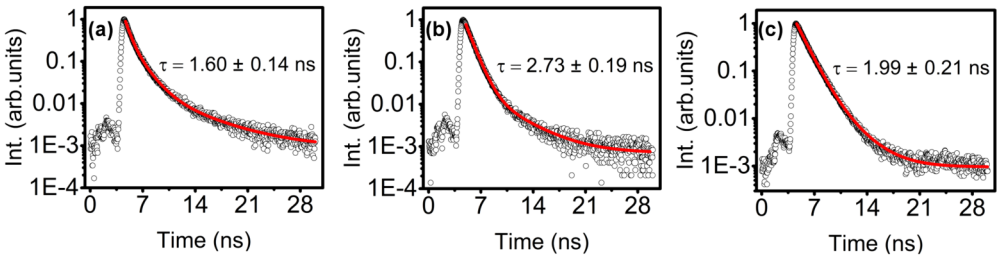

FIG. 2. PL decay time measurements of quantum emitters in GaN obtained at 4 K using a 532-nm pulsed excitation laser. (a)–(c). Double-exponential fits (red line) of the background-corrected measurements yield excited-state lifetimes of (1.62 ± 0.14), (2.73 ± 0.19), and (1.99 ± 0.22) ns for emitters E1, E2, and E3, respectively.

To obtain lifetime information from emitters E1–E3, time-resolved photoluminescence (PL) measurements were carried out using a 532-nm pulsed excitation laser [Figs. 2(a)–2(c)]. Double-exponential fits (red lines) of the experimental data yielded lifetimes of 1.6, 2.7, and 2.0 ns (where the fast decay component of each fit corresponds to the system response). Based on the measured lifetimes, the calculated Fourier transform limited linewidths Γ of emitters E1, E2, and E3 are 0.4, 0.2, and 0.3 μeV, respectively. These values are roughly three orders of magnitude lower than the measured linewidths presented above for the three emitters. A similar, large deviation in the natural linewidth has been reported previously in off-resonantly excited single GaN and InGaN QDs, and it is associated with spectral diffusion [37,38]. The major cause for spectral diffusion in QDs is charge fluctuations, which are likely exacerbated in GaN by the large in-built electric field caused by the spontaneous and piezoelectric polarization of GaN [37,39]. Hence, we attribute the ZPL broadening seen in Fig. 1(c) to ultrafast spectral diffusion (at μs- or ns timescales). Ultrafast spectral diffusion has been reported as a mechanism for broadening in other materials such as SiC and diamond [23,40].

To gain more information on ZPL stability, we performed time-resolved spectroscopy [Figs. 3(a)–3(c)]. The mean ZPL peak position for emitters E1–E3, at an excitation power of 50 μW, is (1.7956 ± 0.0002) eV, (1.8517 ± 0.0005) eV, and (1.9809 ± 0.0002) eV, respectively. The emitters do not show substantial spectral diffusion at a timescale of seconds. However, the lines are inhomogeneously broadened most likely due to ultrafast spectral diffusion. Thus, faster (μs to ns) measurements are required to probe the aforementioned ultrafast spectral kinetics [41].

Figs. S4(a)–S4(c) shows the ZPL shift [$\Delta E_{ZPL}(T)$] for the three emitters as a function of temperature, where the shift is calculated as $\Delta E_{ZPL}(T) = E_{ZPL}(T) - E_{ZPL}(4\,K)$ [36]. The emitters exhibit the previously reported, unusual S-shape (inverted S-shape) dependence of the ZPL on temperature [33]. Also, consistent with the previous study, the temperature-dependent broadening of the FWHM for E1–E3 shown in Figs. S4(d)–S4(f) deviates from the monotonic temperature dependence that is typical of simple defect systems [23,41,42].

Next, we investigate the photophysics of multiple emitters at RT. We measured the brightness of ten SPEs and extracted the maximum fluorescence intensity of each emitter. Figure 4(a) shows an example of background-corrected, power-dependent saturation behavior for a representative emitter in GaN. It has a RT ZPL at 1.818 eV for optimized absorption polarization direction. The power-dependent emission intensities are fitted using the relationship

$$I = I_\infty \frac{P}{P + P_{sat}}, \tag{2}$$

where I_∞ is the maximum intensity and P_{sat} is the saturation power, yielding ∼105 kCounts/s and ∼ 558 μW, for the representative emitter. The power-dependent increase in the signal and background count is compared in Fig. S5 [36]. The histograms in Figs. 4(b) and 4(c) summarize the maximum intensity and saturation power for eight additional emitters under optimized absorption polarization condition. The mean value of maximum intensity I_∞ is (427 ± 215) kCounts/s,

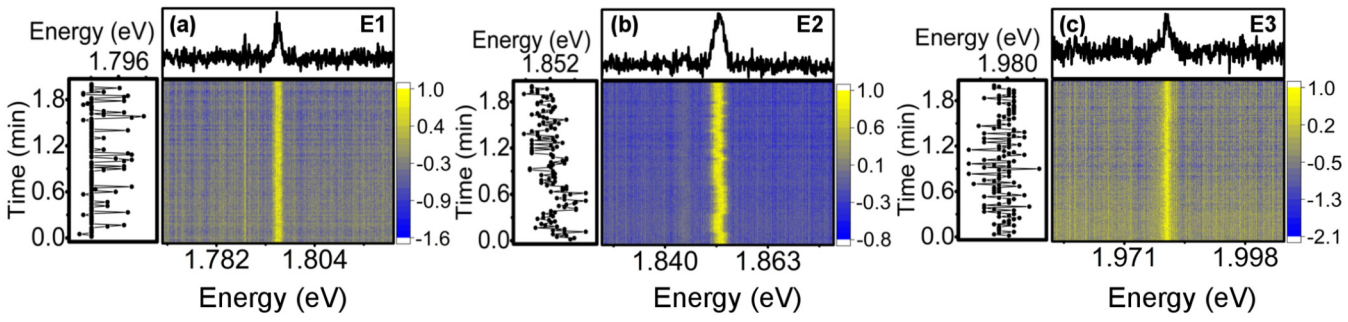

FIG. 3. Time-resolved PL spectra of the emitters E1–E3 obtained at 4 K using an excitation power of 50 μW. (a)–(c) ZPL peak energy (left) measured every second for 2 min. The spectral maps show the bright yellow points as the peaks of the ZPL corresponding to the integrated spectrum (top) for each emitter. A stable mean ZPL peak energy of (1.796 ± 0.0002) eV, (1.852 ± 0.0005) eV, and (1.981 ± 0.0002) eV is observed for E1, E2, and E3, respectively.

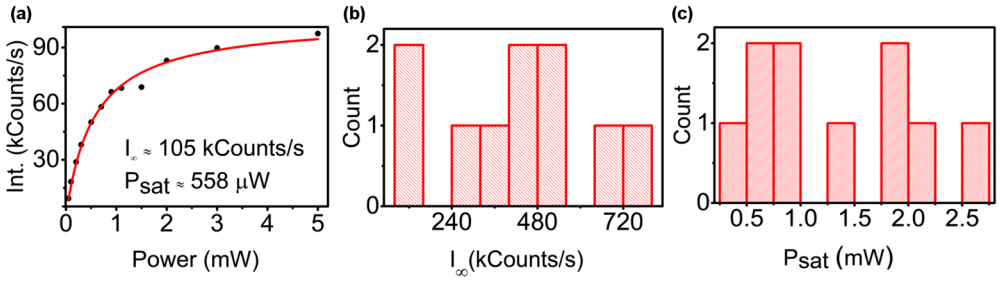

FIG. 4. Saturation behavior of emitters in GaN at room temperature. (a) Background-corrected fluorescence intensity versus power from a representative emitter with a ZPL at 1.818 eV, and a maximum intensity of $\sim$ 105 kCounnts/s at a saturation power of $\sim$558 μW. (b), (c) Statistical distribution of the maximum intensity and saturation power from eight emitters, with a mean value of (427 ± 215) kCounts/s and (1270 ± 735) μW, respectively.

where all emitters are excited using a 532-nm cw laser. This is comparable to other emitters in 3D crystals and can be further improved by employing solid immersion lenses or nanoscale pillars [24,43–45]. The considerable standard deviation observed in the mean fluorescence intensity, as well as the saturation power, (1270 ± 735) μW, may arise from discrepancies in the effective absorption of the off-resonant excitation by the different emitters due to their multiple orientations in the film, as is discussed below [46].

Given the variability in brightness of different SPEs in GaN, we investigated the power-dependent antibunching characteristics of individual emitters, at different fractions of their respective saturation powers (P_{sat}). Figures S6(a)–S6(c) show power-dependent, second-order autocorrelation functions for another three emitters at RT, with ZPLs at 1.934, 1.818, and 1.826 eV, respectively (see Figs. S7(a)–7(c) in Supplemental Material [36]). The measurements reveal bunching statistics at intermediate timescales for increasing excitation powers, confirming the involvement of shelving states in the transition kinetics at RT. The power-dependent antibunching characteristics are well fitted using a second-order autocorrelation function accounting for a three-level system [Eq. (S1)], i.e., Eq. (1) rewritten in terms of rates. The antibunching (λ_1) and bunching (λ_2) free parameters, as well as bunching measurement factor (a), are determined for each one of the three emitters at different powers. The strength of the bunching behavior at different values of P_{sat} varies between emitters, as expected from the large differences in saturation behaviors discussed above.

By fitting the power-dependent behaviors of λ_1, λ_2, and a for each emitter in Figs. 5(a)–5(c) via a three-level transition kinetics model, we determine the characteristic rate coefficients and relevant parameters (see Supplemental Material [36]). Table II summarizes these values for each emitter together with their corresponding ZPL energy. The nonradiative decay in $\mathbf{E_b}$ and $\mathbf{E_c}$ occurs via a power-dependent shelving mechanism with a positive value for β (see Supplemental Material [36]). On the other hand, the nonradiative decay in $\mathbf{E_a}$ occurs via a power-independent shelving state where $\beta = 0$. The difference in the value of β indicates a varying dependence of absorption cross section for the individual shelving state, with varying excitation power.

The excited state lifetime $\tau_{|2\rangle}$ is calculated for the three emitters using the expression $\tau_{|2\rangle} = (\kappa_{21} + \kappa_{23})^{-1}$ [47]. As shown in Table III, the emitters have short lifetimes with

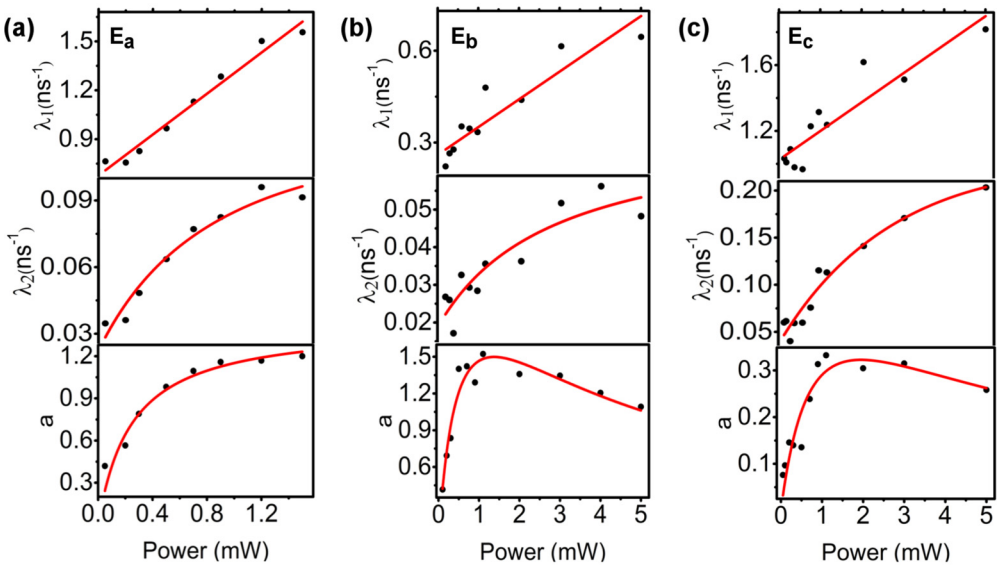

FIG. 5. Power-dependent properties of the free parameters λ_1, λ_2 and the branching ratio of rate coefficients, a, for the three emitters measured at room temperature. The data points (black dots) are fitted well (red lines) by considering three-level transition kinetics.

TABLE II. Rate coefficients extracted for the selected three SPEs by fitting their power-dependent parameters in Fig. S5 [36]. The quantities κ_{12}, κ_{21}, κ_{23}, and κ_{31} are the rate coefficients for transitions between coupled states $|1\rangle \rightarrow |2\rangle$, $|2\rangle \rightarrow |1\rangle$, $|2\rangle \rightarrow |3\rangle$, and $|3\rangle \rightarrow |1\rangle$, respectively (see Supplemental Material, Fig. S5 [36]). All emitters except $\mathbf{E_a}$ show a power-dependent shelving state. α and β are linear fitting parameters for the power dependence of κ_{12} and κ_{31}, respectively.

SPE	ZPL (eV)	κ_{21} (ns^{-1})	κ_{23} (ns^{-1})	κ_{31} (ns^{-1})	κ_{31}^{0} (ns^{-1})	α (μW^{-1})	β (μW^{-1})
$\mathbf{E_a}$	1.934	0.678 ± 0.034	0.127 ± 0.012	0.024 ± 0.005	–	$(9.27 \pm 1.03) \times 10^{-4}$	0
$\mathbf{E_b}$	1.818	0.268 ± 0.031	0.046 ± 0.037	–	0.021 ± 0.004	$(3.31 \pm 0.87) \times 10^{-4}$	$(3.29 \pm 0.21) \times 10^{-5}$
$\mathbf{E_c}$	1.826	1.039 ± 0.047	0.521 ± 0.175	–	0.043 ± 0.007	$(1.65 \pm 0.25) \times 10^{-4}$	$(3.49 \pm 0.41) \times 10^{-4}$

moderate variability between them. The short lifetime is characteristic of all SPEs in GaN as demonstrated before with direct pulsed-laser excitation measurements as well. Also, κ_{21} is 2–40 times larger than κ_{23}, indicating the strong propensity of the excited state to decay radiatively to the ground state, rather than via the "dark" shelving state. One of the advantages of the rate analysis, using this approach, is that it allows us to estimate the metastable lifetime ($\tau_{|3\rangle}$) separately from the excited state lifetime. The quantity $\tau_{|3\rangle}$ is given by $1/\kappa_{31}$ or $1/\kappa_{31}^{0}$ in the case of a power-dependent shelving state [47].

Finally, we focus on the polarization behavior of emitters at RT. Figure 6(a) shows a polar plot from a representative emitter with a RT ZPL at 1.818 eV. The absorption polarization [green] profile is traced using a half-wave plate to highlight the angle at which the minimum and maximum intensities occur. By fixing the half-wave plate at an angle where maximum absorption intensity occurs, and rotating the visible polarizer, we obtain the emission polarization profile for the representative emitters (red) in Fig. 6(a). The polarization data are fitted with the function $I(\varphi) = a + b\cos^2(\varphi)$, where a, b, and ϕ are offset parameter, initial intensity amplitude, and angle between excitation and dipole orientation, respectively [48]. Fitting the emission polarization with this function, we determine the minimum [$I_{\min} = I(\varphi = 90^\circ) = a$] and maximum [$I_{\max} = I(\varphi = 0) = a + b$] of the emission (absorption) polarization direction for the representative emitter in Fig. 6(a) to occur at $\sim$135° (60°) and $\sim$40° (140°), respectively. Such analysis of polar plots is useful as it allows for the easy determination of the dipole polarization visibility, as well as the relative orientations of the absorption and emission polarization for individual emitters [49–51].

The polarization visibility is given by the intensity contrast equation:

$$I = \frac{I_{\max} - I_{\min}}{I_{\max} + I_{\min}}, \tag{3}$$

which, with regard to the emitter shown in Fig. 6(a), yields values for the absorption and emission polarization visibility of 34 and 79%. Notably the absorption is not fully polarized, while the emission is. We carried out similar measurements on 14 additional emitters. Figure 6(b) shows the histogram of their percentile visibility in absorption (green) and emission (red). Interestingly, we observe a significant discrepancy in absorption polarization visibility, which ranges between 26 and 94% with the mean value at (57 ± 26)%. The rather large distribution in absorption dipole visibility results in the large distribution of laser power required to saturate the emitters, as discussed before. This significant difference in excitation visibility as well as saturation behavior indicates that the orientation of the dipole varies from emitter to emitter, with weak visibility being likely the result of the dipole having significant out-of-plane components in the 3D crystal [48,51].

On the other hand, a mean emission polarization visibility of (91 ± 11)% is obtained for the same emitters. This visibility is a strong indicator that these emitters in GaN are linearly polarized (ideal case ~100% for a single dipole). We attribute the deviation from the ideal value of the visibility to fluorescence aberrations arising from residual birefringence and imaging through a high-NA (0.9) objective [48,52].

The relative orientation between the absorption and the emission dipoles is further analyzed for the 14 emitters showing a misalignment ranging from 0 to 120° as shown

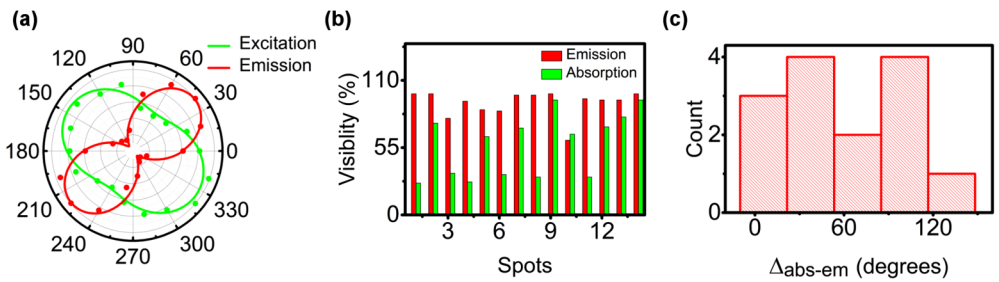

FIG. 6. Room-temperature polarization spectroscopy of emitters in GaN. (a) Absorption (green) and emission (red) polarization profiles from an emitter with a ZPL at 1.818 eV, exhibiting polarization visibilities of 34 and 79%, respectively. (b) Polarization visibilities of 14 emitters showing that while the emitters are strongly polarized in emission, they show variable degrees of absorption polarization. (c) Histogram of the difference in orientation between absorption and emission polarization.

TABLE III. Calculated values of excited-state ($\tau_{|2\rangle}$) and metastable-state lifetime ($\tau_{|3\rangle}$) for the three emitters.

	E_a	E_b	E_c
$\tau_{\|2\rangle}$ (ns)	1.24 ± 0.07	3.19 ± 0.79	0.64 ± 0.09
$\tau_{\|3\rangle}$ (ns)	41.7 ± 8.7	47.6 ± 9.1	23.3 ± 3.8

by the histogram in Fig. 6(c). This is expected, considering that the emitters are believed to be point defects located in cubic inclusions. Consequently, for off-resonant excitation, absorption may involve a transition to an excited state of the inclusion. The emission transition, however, involves only the highly localized levels of the defect, thus giving a more distinct radial emission direction compared to that of absorption.

To elucidate the nature of the preferential excitation axis, the maximum absorption polarization angle is measured for the 14 emitters and compared to the wurtzite crystal plane directions in Fig. 7. The angle spans all directions, with a maximum occurrence at ∼140°, which corresponds to the [1$\bar{1}$00] lattice direction of the (0001) wurtzite GaN, as shown in Fig. 7(b). The rotational orientation of the sample was deduced by considering that the sample is mounted with the unit cell along the (0001) plane almost parallel to the excitation field. In this arrangement, rotating the excitation polarization through 180° sweeps all planes of the hexagonal unit cell. Hence the highest occurrence angle of 140°, which corresponds to the lattice plane direction [1$\bar{1}$00], is believed to contain the greatest density of cubic inclusions. Furthermore, the highest absorption visibility of 94% is observed from an emitter with an orientation angle of ∼16°, which corresponds to a minimal out-of-plane orientation. This is expected since confined exciton separation occurs along the *c* axis, where the excitation is aligned parallel to the *c* axis [53].

IV. CONCLUSION

To conclude, we carried out low-temperature spectroscopy of SPEs in GaN. While the FWHM of GaN emitters is significantly narrower at 4 K than at RT, the FWHM does not approach the Fourier transform limited linewidths. Ultrafast spectral diffusion is the most likely explanation for the line broadening where future experimental investigation using

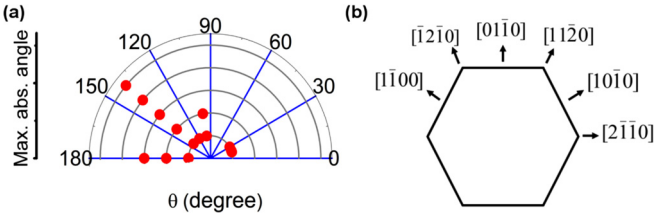

FIG. 7. Maximum absorption angles for the 14 emitters shown in Fig. 6. (a) Scatter plot of the maximum absorption axis of the 14 emitters. (b) Fundamental lattice directions of the wurtzite unit cell, showing that the maximum in angular distribution in (a) corresponds to the [1$\bar{1}$00] lattice direction of wurtzite GaN.

approaches such as correlation interferometery should confirm this hypothesis [40]. Temperature-dependent ZPL shift and FWHM broadening results confirm the previously proposed explanation for the existence of a cubic inclusion near the radiative point defect as the cause for the observed S-shaped ZPL shift and nonmonotonic broadening.

A saturation behavior of the emitters was also measured, showing brightness difference among emitters with an average saturation count rate of (427 ± 215) kCounts/s. The emitters' kinetics can be described efficiently using a three-level system. Polarization measurements from multiple emitters show high emission visibility of more than 90% and varying strength in the absorption cross section under excitation with a linearly polarized, off-resonant laser. This work evaluates SPEs in GaN as strong alternatives for application in quantum technologies; at the same time, it highlights bottlenecks hindering their immediate implementation.

ACKNOWLEDGMENTS

This work was supported in part by the US Army Research Laboratory (ARL) (Grant No. FA9550-14-1-0052) and the Air Force Office of Scientific Research (AFOSR) (Grant No. FA9550-14-1-0052). Financial support from the Australian Research Council (via Grants No. DP140102721 and No. DP180100077), FEI Company, the Asian Office of Aerospace Research and Development (Grant No. FA2386-17-1-4064), and the Office of Naval Research Global (Grant No. N62909-18-1-2025) are gratefully acknowledged.

[1] M. Fiorentino, P. L. Voss, J. E. Sharping, and P. Kumar, All-fiber photon-pair source for quantum communications, IEEE Photonics Technol. Lett. **14**, 983 (2002).

[2] C. H. Bennett, G. Brassard, and N. D. Mermin, Quantum Cryptography without Bell's Theorem, Phys. Rev. Lett. **68**, 557 (1992).

[3] C. Simon, H. de Riedmatten, M. Afzelius, N. Sangouard, H. Zbinden, and N. Gisin, Quantum Repeaters with Photon Pair Sources and Multimode Memories, Phys. Rev. Lett. **98**, 190503 (2007).

[4] H.-J. Briegel, W. Dür, J. I. Cirac, and P. Zoller, Quantum Repeaters: The Role of Imperfect Local Operations in Quantum Communication, Phys. Rev. Lett. **81**, 5932 (1998).

[5] J. R. Weber, W. F. Koehl, J. B. Varley, A. Janotti, B. B. Buckley, C. G. Van de Walle, and D. D. Awschalom, Quantum computing with defects, Proc. Natl. Acad. Sci. USA **107**, 8513 (2010).

[6] T. D. Ladd, F. Jelezko, R. Laflamme, Y. Nakamura, C. Monroe, and J. L. O'Brien, Quantum computers, Nature (London) **464**, 45 (2010).

[7] L. Childress and R. Hanson, Diamond NV centers for quantum computing and quantum networks, MRS Bull. **38**, 134 (2013).

[8] N. Montaut, L. Sansoni, E. Meyer-Scott, R. Ricken, V. Quiring, H. Herrmann, and C. Silberhorn, High-Efficiency Plug-and-Play Source of Heralded Single Photons, Phys. Rev. Appl. **8**, 024021 (2017).

[9] A. S. Solntsev, F. Setzpfandt, A. S. Clark, C. W. Wu, M. J. Collins, C. Xiong, A. Schreiber, F. Katzschmann, F. Eilenberger, R. Schiek *et al.*, Generation of Nonclassical Biphoton States Through Cascaded Quantum Walks on a Nonlinear Chip, Phys. Rev. X **4**, 031007 (2014).

[10] J. C. Loredo, N. A. Zakaria, N. Somaschi, C. Anton, L. De Santis, V. Giesz, T. Grange, M. A. Broome, O. Gazzano, and G. Coppola, Scalable performance in solid-state single-photon sources, Optica **3**, 433 (2016).

[11] N. Somaschi, V. Giesz, L. De Santis, J. C. Loredo, M. P. Almeida, G. Hornecker, S. L. Portalupi, T. Grange, C. Antón, and J. Demory, Near-optimal single-photon sources in the solid state, Nat. Photonics **10**, 340 (2016).

[12] S. C. Kitson, P. Jonsson, J. G. Rarity, and P. R. Tapster, Intensity fluctuation spectroscopy of small numbers of dye molecules in a microcavity, Phys. Rev. A **58**, 620 (1998).

[13] B. Lounis and W. E. Moerner, Single photons on demand from a single molecule at room temperature, Nature (London) **407**, 491 (2000).

[14] I. Aharonovich, D. Englund, and M. Toth, Solid-state single-photon emitters, Nat. Photonics **10**, 631 (2016).

[15] X. He, N. F. Hartmann, X. Ma, Y. Kim, R. Ihly, J. L. Blackburn, W. Gao, J. Kono, Y. Yomogida, and A. Hirano, Tunable room-temperature single-photon emission at telecom wavelengths from sp^3 defects in carbon nanotubes, Nat. Photonics **11**, 577 (2017).

[16] A. Migdall, S. V. Polyakov, J. Fan, and J. C. Bienfang, *Single-Photon Generation and Detection: Physics and Applications* (Academic, New York, 2013).

[17] S. Buckley, K. Rivoire, and J. Vučković, Engineered quantum dot single-photon sources, Rep. Prog. Phys. **75**, 126503 (2012).

[18] A. Sipahigil, R. E. Evans, D. D. Sukachev, M. J. Burek, J. Borregaard, M. K. Bhaskar, C. T. Nguyen, J. L. Pacheco, H. A. Atikian, C. Meuwly, R. M. Camacho, F. Jelezko, E. Bielejec, H. Park, M. Lončar, and M. D. Lukin, An integrated diamond nanophotonics platform for quantum-optical networks, Science **354**, 847 (2016).

[19] M. K. Bhaskar, D. D. Sukachev, A. Sipahigil, R. E. Evans, M. J. Burek, C. T. Nguyen, L. J. Rogers, P. Siyushev, M. H. Metsch, H. Park, F. Jelezko, M. Lončar, and M. D. Lukin, Quantum Nonlinear Optics with a Germanium-Vacancy Color Center in a Nanoscale Diamond Waveguide, Phys. Rev. Lett. **118**, 223603. (2017).

[20] K. Bray, R. Sandstrom, C. Elbadawi, M. Fischer, M. Schreck, O. Shimoni, C. Lobo, M. Toth, and I. Aharonovich, Localization of narrowband single photon emitters in nanodiamonds, ACS Appl. Mater. Interfaces **8**, 7590 (2016).

[21] I. Aharonovich and E. Neu, Diamond nanophotonics, Adv. Opt. Mater. **2**, 911 (2014).

[22] D. J. Christle, P. V. Klimov, C. F. de las Casas, K. Szász, V. Ivády, V. Jokubavicius, J. Ul Hassan, M. Syväjärvi, W. F. Koehl, T. Ohshima, N. T. Son, E. Janzén, Á. Gali, and D. D. Awschalom, Isolated Spin Qubits in SiC with a High-Fidelity Infrared Spin-to-Photon Interface, Phys. Rev. X **7**, 021046 (2017).

[23] B. Lienhard, T. Schröder, S. Mouradian, F. Dolde, T. T. Tran, I. Aharonovich, and D. Englund, Bright and photostable single-photon emitter in silicon carbide, Optica **3**, 768 (2016).

[24] M. Widmann, S. Y. Lee, T. Rendler, N. T. Son, H. Fedder, S. Paik, L. P. Yang, N. Zhao, S. Yang, I. Booker, A. Denisenko, M. Jamali, S. A. Momenzadeh, I. Gerhardt, T. Ohshima, A. Gali, E. Janzen, and J. Wrachtrup, Coherent control of single spins in silicon carbide at room temperature, Nat. Mater. **14**, 164 (2015).

[25] S. Castelletto, B. Johnson, V. Ivády, N. Stavrias, T. Umeda, A. Gali, and T. Ohshima, A silicon carbide room-temperature single-photon source, Nat. Mater. **13**, 151 (2014).

[26] S. Choi, B. C. Johnson, S. Castelletto, C. Ton-That, M. R. Phillips, and I. Aharonovich, Single photon emission from ZnO nanoparticles, Appl. Phys. Lett. **104**, 261101 (2014).

[27] O. Neitzke, A. Morfa, J. Wolters, A. W. Schell, G. n. Kewes, and O. Benson, Investigation of line width narrowing and spectral jumps of single stable defect centers in ZnO at cryogenic temperature, Nano Lett. **15**, 3024 (2015).

[28] A. J. Morfa, B. C. Gibson, M. Karg, T. J. Karle, A. D. Greentree, P. Mulvaney, and S. Tomljenovic-Hanic, Single-photon emission and quantum characterization of zinc oxide defects, Nano Lett. **12**, 949 (2012).

[29] T. T. Tran, K. Bray, M. J. Ford, M. Toth, and I. Aharonovich, Quantum emission from hexagonal boron nitride monolayers, Nat. Nanotechnol. **11**, 37 (2016).

[30] S. Deshpande, J. Heo, A. Das, and P. Bhattacharya, Electrically driven polarized single-photon emission from an InGaN quantum dot in a GaN nanowire, Nat. Commun. **4**, 1675 (2013).

[31] M. J. Holmes, K. Choi, S. Kako, M. Arita, and Y. Arakawa, Room-temperature triggered single photon emission from a III-nitride site-controlled nanowire quantum dot, Nano Lett. **14**, 982 (2014).

[32] B. Demory, T. A. Hill, C.-H. Teng, L. Zhang, H. Deng, and P.-C. Ku, Plasmonic enhancement of single photon emission from a site-controlled quantum dot, ACS Photonics **2**, 1065 (2015).

[33] A. M. Berhane, K.-Y. Jeong, Z. Bodrog, S. Fiedler, T. Schröder, N. V. Triviño, T. Palacios, A. Gali, M. Toth, D. Englund, and I. Aharonovich, Bright room-temperature single-photon emission from defects in gallium nitride, Adv. Mater. **29**, 1605092 (2017).

[34] A. M. Berhane, C. Bradac, and I. Aharonovich, Photoinduced blinking in a solid-state quantum system, Phys. Rev. B **96**, 041203 (2017).

[35] Y. Zhou, Z. Wang, A. Rasmita, S. Kim, A. Berhane, Z. Bodrog, G. Adamo, A. Gali, I. Aharonovich, and W.-b. Gao, Room temperature solid-state quantum emitters in the telecom range, Sci. Adv. **4**, eaar3580 (2018).

[36] See Supplemental Material at http://link.aps.org/supplemental/10.1103/PhysRevB.97.165202 for supporting data and analysis of transition kinetics.

[37] S. Kako, K. Hoshino, S. Iwamoto, S. Ishida, and Y. Arakawa, Exciton and biexciton luminescence from single hexagonal GaN/AlN self-assembled quantum dots, Appl. Phys. Lett. **85**, 64. (2004).

[38] M. Bayer and A. Forchel, Temperature dependence of the exciton homogeneous linewidth in In 0.60 Ga 0.40 As/GaAs self-assembled quantum dots, Phys. Rev. B **65**, 041308 (2002).

[39] M. Arita, F. Le Roux, M. J. Holmes, S. Kako, and Y. Arakawa, Ultraclean single photon emission from a GaN quantum dot, Nano Lett. **17**, 2902 (2017).

[40] J. Wolters, N. Sadzak, A. W. Schell, T. Schröder, and O. Benson, Measurement of the Ultrafast Spectral Diffusion of the Optical Transition of Nitrogen Vacancy Centers in Nano-Size Diamond Using Correlation Interferometry, Phys. Rev. Lett. **110**, 027401 (2013).

[41] E. Neu, C. Hepp, M. Hauschild, S. Gsell, M. Fischer, H. Sternschulte, D. Steinmüller-Nethl, M. Schreck, and C. Becher,

Low-temperature investigations of single silicon vacancy colour centres in diamond, New J. Phys. **15**, 043005 (2013).

[42] N. R. Jungwirth, B. Calderon, Y. Ji, M. G. Spencer, M. E. Flatté, and G. D. Fuchs, Temperature dependence of wavelength selectable zero-phonon emission from single defects in hexagonal boron nitride, Nano Lett. **16**, 6052 (2016).

[43] J. Hadden, J. Harrison, A. Stanley-Clarke, L. Marseglia, Y.-L. Ho, B. Patton, J. O'Brien, and J. Rarity, Strongly enhanced photon collection from diamond defect centers under microfabricated integrated solid immersion lenses, Appl. Phys. Lett. **97**, 241901 (2010).

[44] B. J. Hausmann, T. M. Babinec, J. T. Choy, J. S. Hodges, S. Hong, I. Bulu, A. Yacoby, M. D. Lukin, and M. Lončar, Single-color centers implanted in diamond nanostructures, New J. Phys. **13**, 045004 (2011).

[45] T. T. Tran, C. Zachreson, A. M. Berhane, K. Bray, R. G. Sandstrom, L. H. Li, T. Taniguchi, K. Watanabe, I. Aharonovich, and M. Toth, Quantum Emission from Defects in Single-Crystalline Hexagonal Boron Nitride, Phys. Rev. Appl. **5**, 034005 (2016).

[46] E. Neu, M. Agio, and C. Becher, Photophysics of single silicon vacancy centers in diamond: Implications for single photon emission, Opt. Express **20**, 19956 (2012).

[47] N. Jungwirth, Y. Pai, H. Chang, E. MacQuarrie, K. Nguyen, and G. Fuchs, A single-molecule approach to ZnO defect studies: Single photons and single defects, J. Appl. Phys. **116**, 043509 (2014).

[48] N. R. Jungwirth, H.-S. Chang, M. Jiang, and G. D. Fuchs, Polarization spectroscopy of defect-based single photon sources in ZnO, ACS Nano **10**, 1210 (2015).

[49] E. Neu, M. Fischer, S. Gsell, M. Schreck, and C. Becher, Fluorescence and polarization spectroscopy of single silicon vacancy centers in heteroepitaxial nanodiamonds on iridium, Phys. Rev. B **84**, 205211 (2011).

[50] I. Aharonovich, S. Castelletto, B. C. Johnson, J. C. McCallum, D. A. Simpson, A. D. Greentree, and S. Prawer, Chromium single-photon emitters in diamond fabricated by ion implantation, Phys. Rev. B **81**, 121201(R) (2010).

[51] A. L. Exarhos, D. A. Hopper, R. R. Grote, A. Alkauskas, and L. C. Bassett, Optical signatures of quantum emitters in suspended hexagonal boron nitride, ACS Nano **11**, 3328 (2017).

[52] J. T. Fourkas, Rapid determination of the three-dimensional orientation of single molecules, Opt. Lett. **26**, 211 (2001).

[53] A. Lohrmann, N. Iwamoto, Z. Bodrog, S. Castelletto, T. Ohshima, T. J. Karle, A. Gali, S. Prawer, J. C. McCallum, and B. C. Johnson, Single-photon emitting diode in silicon carbide, Nat. Commun. **6**, 7783 (2015).